



AIAA 2002-2580

**A Comparison of
Ffowcs Williams-Hawkings Solvers
for Airframe Noise Applications**

David P. Lockard
NASA Langley Research Center
Hampton, VA 23681

8th AIAA/CEAS Aeroacoustics Conference
June 17-19, 2002
Breckenridge, CO

A COMPARISON OF FFWCS WILLIAMS-HAWKINGS SOLVERS FOR AIRFRAME NOISE APPLICATIONS

David P. Lockard*
NASA Langley Research Center
Hampton, VA

This paper presents a comparison between two implementations of the Ffowcs Williams and Hawkings equation for airframe noise applications. Airframe systems are generally moving at constant speed and not rotating, so these conditions are used in the current investigation. Efficient and easily implemented forms of the equations applicable to subsonic, rectilinear motion of all acoustic sources are used. The assumptions allow the derivation of a simple form of the equations in the frequency-domain, and the time-domain method uses the restrictions on the motion to reduce the work required to find the emission time. The comparison between the frequency domain method and the retarded time formulation reveals some of the advantages of the different approaches. Both methods are still capable of predicting the far-field noise from nonlinear near-field flow quantities. Because of the large input data sets and potentially large numbers of observer positions of interest in three-dimensional problems, both codes utilize the message passing interface to divide the problem among different processors. Example problems are used to demonstrate the usefulness and efficiency of the two schemes.

Nomenclature

c_o	ambient speed of sound
f	integration surface defined by $f = 0$
F_i	dipole source terms
H	Heaviside function
i	$\sqrt{-1}$
M_i	local source Mach number vector, v_i/c
M	Mach number, $ M_i $
\hat{n}_i	Outward directed unit normal vector
p	pressure
\mathbf{Q}	monopole source term
Q_i	components of vector in Eq.(6)
Q_n	$Q_i \hat{n}_i$
r_i	radiation vector, $x_i - \xi_i$
r	magnitude of radiation vector, $ r_i $
t	time
u_i	Cartesian fluid velocity components

v_i	Cartesian surface velocity components
x, y, z	Cartesian observer coordinates

Greek:

α_1, α_2	mapped surface coordinates
β	$\sqrt{1 - M^2}$
$\delta(f)$	Dirac delta function
δ_{ij}	Kronecker delta
ρ	fluid density
τ	retarded or emission time, $t - r/c_o$
ξ, η, ζ	Source coordinates

Superscript:

'	perturbation quantity (e.g. $\rho' = \rho - \rho_o$)
$\hat{}$	unit vector
$\dot{}$	time derivative

Subscript:

e	emission or retarded quantity
o	freestream quantity
r	inner product with \hat{r}_i
ret	quantity evaluated at retarded time τ
n	inner product with \hat{n}_i

Introduction

Despite recent advances in computational aeroacoustics, numerical simulations that resolve wave propagation from near-field sources to far-field observers are still prohibitively expensive and often infeasible. Integral techniques that can predict the far-field signal based solely on near-field input are a means to overcome this difficulty.

The Ffowcs Williams and Hawkings¹ (FW-H) equation is a rearrangement of the exact continuity and Navier-Stokes equations. The time histories of all the flow variables are needed, but no spatial derivatives are explicitly required. The solution to the FW-H equation requires a surface and a volume integral, but the solution is often well approximated by the surface integral alone. Singer *et al.*² and Brentner and Farassat³ have shown that when the surface is in the near field of a solid body, the FW-H approach correctly filters out the part of the solution that does not radiate as sound, whereas the Kirchhoff method produces erroneous results. Many applications of the FW-H and Kirchhoff methods can be found in the area of rotorcraft acoustics.⁴⁻⁷ The FW-H method has typically been applied

*Research Scientist, Senior Member, AIAA

Copyright © 2002 by the American Institute of Aeronautics and Astronautics, Inc. No copyright is asserted in the United States under Title 17, U.S. Code. The U.S. Government has a royalty-free license to exercise all rights under the copyright claimed herein for Governmental Purposes. All other rights are reserved by the copyright owner.

by having the integration surface coincide with solid bodies, but the method is still applicable when the surface is off the body and permeable. The codes developed in this work are valid for both cases.

For three-dimensional flows, the time-domain FW-H formulations developed by Farassat⁸ are efficient and amenable to numerical computations. Some simplifications are applied here based on restrictions of the surface motion, but the development follows that of Farassat very closely. The frequency-domain version of the FW-H uses the form of the equations developed by Lockard⁹ for two-dimensional problems. However, the derivation was done using Cartesian tensor notation, and is equally valid in three-dimensions as long as the appropriate Green function is employed.

The remainder of the paper describes the time- and frequency-domain formulations in enough detail to show the similarities and differences between the methods. A discussion of various parallelization strategies follows. Finally, two example problems are used to demonstrate the utility and efficiency of the schemes. The last example involves a noise calculation based on a large-scale CFD computation of a landing gear.

Governing Equations

The FW-H equation can be written in differential form¹⁰ as

$$\begin{aligned} \left(\frac{\partial^2}{\partial t^2} - c_o^2 \frac{\partial^2}{\partial x_i \partial x_i} \right) \left(H(f) \rho' \right) = \\ \frac{\partial^2}{\partial x_i \partial x_j} \left(T_{ij} H(f) \right) \\ - \frac{\partial}{\partial x_i} \left(F_i \delta(f) \right) + \frac{\partial}{\partial t} \left(Q \delta(f) \right) \end{aligned} \quad (1)$$

where

$$T_{ij} = \rho u_i u_j + P_{ij} - c_o^2 \rho' \delta_{ij}, \quad (2)$$

$$F_i = \left(P_{ij} + \rho u_i (u_j - v_j) \right) \frac{\partial f}{\partial x_j}, \quad \text{and} \quad (3)$$

$$Q = \left(\rho_o v_i + \rho (u_i - v_i) \right) \frac{\partial f}{\partial x_i}. \quad (4)$$

The contribution of the Lighthill stress tensor, T_{ij} , to the right-hand side is known as the quadrupole term. The dipole term F_i involves an unsteady force, and Q gives rise to a monopole-type contribution that can be thought of as an unsteady mass addition. The function $f = 0$ defines the surface outside of which the solution is desired. The normalization $|\nabla f| = 1$ is used for f . The total density and pressure are given by ρ and p , respectively. The fluid velocities are u_i , while the v_i represent the velocities of the surface f . The Kronecker delta, δ_{ij} , is unity for $i = j$ and zero otherwise. The ambient speed of sound is denoted

by c_o . A prime is used to denote a perturbation quantity relative to the free-stream conditions denoted by the subscript o . The Cartesian coordinates and time are x_i and t , respectively. The usual convention, which is followed here, involves a quiescent ambient state with f prescribed as a function of time so that it always surrounds a moving source region of interest. $H(f)$ is the Heaviside function which is unity for $f > 0$ and zero for $f < 0$. The derivative of the Heaviside function $H'(f) = \delta(f)$ is the Dirac delta function, which is zero for $f \neq 0$, but yields a finite value when integrated over a region including $f = 0$. The inviscid part, $P_{ij} = p \delta_{ij}$, of the compressive stress tensor P_{ij} is used in this work.

Equation 1 is typically solved using a Green function technique. The temporal and spatial convolution of the free-space Green function with the source terms yields the solution for ρ' . In the farfield, $\rho' = c_o^2 \rho'$. The three-dimensional Green function¹⁰ is

$$G(x_i, t; \xi_i, \tau) = \frac{\delta(\tau - t + r/c_o)}{4\pi r} \quad (5)$$

where $r_i = x_i - \xi_i$ is the radiation vector, and $r = |r_i|$. Because of the delta function, the solution to equation 1 can be manipulated into various forms, some of which are amenable to numerical solution such as formulation 1A of Farassat.⁸ An alternative approach is to solve the FW-H equation in the frequency domain. In this work we follow the frequency-domain approach of Lockard⁹ that is restricted to uniform, rectilinear motion, but other methods can be used that still allow general motion. In the following sections, the current implementations of these methods are discussed.

Time-Domain Method

A concise, time-domain solution to equation 1 that is applicable to nondeforming, porous surfaces can be obtained from the derivation of Farassat¹¹ using the variables

$$\begin{aligned} Q_i &= (\rho_o - \rho) v_i + \rho u_i, \quad \text{and} \\ L_i &= p \hat{n}_i + \rho u_i (u_j - v_j) \hat{n}_j \end{aligned} \quad (6)$$

as proposed by Di Francescantonio.⁶ The integral solution is given by

$$\begin{aligned} 4\pi \rho' (x_i, t) = \\ \int_{f=0} \left[\frac{\dot{Q}_j \hat{n}_j}{r(1-M_r)^2} + \frac{Q_j \hat{n}_j (r \dot{M}_r + c_o (M_r - M^2))}{r^2 (1-M_r)^3} \right]_{\text{ret}} ds \\ + \int_{f=0} \left[\frac{\dot{L}_j \hat{r}_j}{c_o r (1-M_r)^2} + \frac{L_j \hat{r}_j - L_i M_i}{r^2 (1-M_r)^2} \right]_{\text{ret}} ds \\ + \int_{f=0} \left[\frac{L_j \hat{r}_j (r \dot{M}_j \hat{r}_j + c_o (M_j \hat{r}_j - M^2))}{c_o r^2 (1-M_r)^3} \right]_{\text{ret}} ds + p'_Q \end{aligned} \quad (7)$$

where p'_Q is the quadrupole term, which is neglected in this work. $M_i = v_i/c_o$ is the local Mach number vector, and the superscripted caret ($\hat{\cdot}$) denotes a unit vector. The outward directed unit normal vector is given by \hat{n}_i . The subscript ret denotes evaluation at the retarded or emission time τ . For uniform, rectilinear motion, the normals are not functions of time, so finding $Q_n = Q_i \hat{n}_i$ and $\dot{Q}_i \hat{n}_i$ is sufficient because $\partial/\partial t(Q_n) = \hat{n}_i \partial/\partial t(Q_i) + Q_i \partial/\partial t(\hat{n}_i) = \dot{Q}_i \hat{n}_i$. The dot above a variable indicates a time derivative. Hence, only four variables and their time derivatives are required to compute the kernel functions in equation 7. The time derivatives are computed using fourth-order, central differences. In the current application, the coordinates of the surface and the flow field data are known at the grid points of meshes on a series of surface patches that comprise the complete, closed surface surrounding all sources. The normals are determined using the grid metrics on the patches, which are computed using fourth-order, central differences. Because each surface patch has two independent indices, only two variables (α_1, α_2) are required to describe the variation on the mapped surface. The normal is computed from the outer product

$$n_i = \left\{ \frac{\partial x}{\partial \alpha_1}, \frac{\partial y}{\partial \alpha_1}, \frac{\partial z}{\partial \alpha_1} \right\} \times \left\{ \frac{\partial x}{\partial \alpha_2}, \frac{\partial y}{\partial \alpha_2}, \frac{\partial z}{\partial \alpha_2} \right\}. \quad (8)$$

Whether the normal points inward or outward is dependent on the ordering of the data. The current code reads a file which either specifies a source point within each surface or the correct sign of the normal on each surface. When the surfaces come from CFD data, it is usually possible to deduce which direction the normal will point. However, a visual inspection of the normals is always a good practice because incorrect signs are common and can cause errors that are difficult to recognize.

One of the more computationally intensive parts of a time-domain calculation is the determination of the retarded time τ . For general motion, a root-finding technique must be employed. However, for uniform, rectilinear, subsonic motion, the Garrick triangle¹² uniquely determines the emission time as

$$\begin{aligned} r_e &= \frac{r}{1 - M^2} \left(M \cos(\theta) + \sqrt{1 - M^2 \sin^2(\theta)} \right) \\ \tau &= t - r_e/c_o \end{aligned} \quad (9)$$

where r_e is the distance between the source and the observer at the time of emission τ . The angle between the surface velocity vector v_i and the radiation vector r_i is θ . The $\cos(\theta)$ can be determined from the inner product of the vectors. The variables Q_n , L_i and their time derivatives must then be interpolated to the retarded time. This is an intensive part of the calculation because the interpolation is performed for every grid point, retarded time, and observer position. Changing the indexing of data to increase cache

reuse, loop unrolling, and inlining of the interpolation routine decreased the total run time by half.

Once the kernel functions in equation 7 have been determined, Gaussian quadrature is used to perform the spatial integration over the surface. Because this integration is performed repeatedly for each observer and retarded time, parts of the integral that are independent of time and observer position are precalculated and stored. The integration is performed by linearly interpolating the data from the four corners of each cell using three-dimensional shape functions commonly employed in finite elements.¹³ Defining the mapped coordinates as (α_1, α_2) , the elemental area, dS , is the magnitude of the normal as specified in equation 8. The value of the elemental area at each Gaussian quadrature point is then stored for reuse. The values of the shape functions at each of the quadrature points are also precalculated and stored. Typically, only four quadrature points are required over each cell. Four points will integrate quadratic functions exactly. Although the function being integrated may be of higher order, a quadratic approximation is usually sufficient provided the surface shape is well behaved. Additional quadrature points and higher-order reconstructions within each cell have not been found to be very beneficial. Part of the reason may be the oscillatory nature of the kernel function. The integration of a linear approximation of a sinusoid is often not much different from the quadrature of a higher-order fit. Grid refinement is typically much more influential on the solution quality than the order of the integration.

Because of the need to sample the source data at the retarded time, one cannot arbitrarily choose observer times. A separate code was written to determine the valid range of observer times based on a given range of input data. The Garrick triangle¹² can be used to uniquely determine the minimum and maximum reception times using equations 9 to solve for t given τ .

Impenetrable Surfaces

In many practical applications, the data for the FWH solver is obtained on solid surfaces, and the equations can be greatly simplified thereby decreasing the computational and memory requirements. The simplifications are especially advantageous for the uniform, rectilinear motion case. For impenetrable surface data, $u_j = v_j$ and equations 6 simplify to

$$Q_i = \rho_o v_i \quad \text{and} \quad L_i = p \hat{n}_i. \quad (10)$$

Note that Q is independent of time. Furthermore, the normals \hat{n}_j are only a function of space. Hence, only the time history of the pressure and its time derivative are needed when the viscous terms are neglected in P_{ij} . All of the source terms are linear, yet the method has been shown to give correct results when the surface data is in the nonlinear near field.² The failings of the Kirchhoff method for

problems with solid surfaces is clearly not due to its source terms being linear, but rather the assumptions used to derive the equation.

Frequency-Domain Method

Several frequency-domain formulations of the FW-H equation have been reported in the literature.¹⁴ Here, the method proposed by Lockard⁹ for two-dimensional flows will be extended to three-dimensions. Although this development is restricted to surfaces in rectilinear motion at constant speed, it is still useful for airframe noise, where these assumptions are usually valid. The motion of the surface is assumed to be governed by $f = f(\mathbf{x} + \mathbf{U}t)$ where the components of \mathbf{U} are constant velocities describing the motion of the surface. An application of the Galilean transformation from (\mathbf{x}, t) to (\mathbf{y}, \bar{t}) ,

$$\begin{aligned} y_i &= x_i + U_i t, \quad \bar{t} = t, \\ \frac{\partial}{\partial x_i} &= \frac{\partial}{\partial y_i}, \quad \frac{\partial}{\partial t} = \frac{\partial}{\partial \bar{t}} + U_i \frac{\partial}{\partial y_i}, \end{aligned} \quad (11)$$

to equation 1 leads to the convected wave equation

$$\begin{aligned} &\left(\frac{\partial^2}{\partial \bar{t}^2} + U_i U_j \frac{\partial^2}{\partial y_i \partial y_j} \right. \\ &+ \left. 2U_i \frac{\partial^2}{\partial y_i \partial \bar{t}} - c_o^2 \frac{\partial^2}{\partial y_i \partial y_i} \right) (H(f)\rho') = \\ &\frac{\partial^2}{\partial y_i \partial y_j} (T_{ij}H(f)) - \frac{\partial}{\partial y_i} (F_i \delta(f)) + \frac{\partial}{\partial \bar{t}} (Q_n \delta(f)) \end{aligned} \quad (12)$$

where, after the transformation, the F_i and Q_n become

$$\begin{aligned} F_i &= \left(p\delta_{ij} + \rho(u_i - U_i)(u_j + U_j) + \rho_o U_i U_j \right) \hat{n}_j, \\ Q_n &= \left(\rho(u_i + U_i) - \rho_o U_i \right) \hat{n}_i. \end{aligned} \quad (13)$$

The Lighthill stress tensor T_{ij} is unchanged, and $f = f(\mathbf{y})$ is now only a function of the spatial coordinates. The surface velocities v_i have been replaced by $-U_i$, which can be inferred from inspection of $f(\mathbf{x} + \mathbf{U}t) = 0$. Note that this implies that the mean flow is in the positive direction (or equivalently that the surface moves in the negative direction) when $U_i > 0$. The v_i used throughout the time-domain formulation are of opposite sign and should not be confused with the U_i . Equation 12 is now in a convenient form to perform the Fourier analysis. With application of the Fourier transform pair

$$\begin{aligned} \mathcal{F}\{q(t)\} &= q(\omega) = \int_{-\infty}^{\infty} q(t) \exp(-i\omega t) dt \quad \text{and} \\ \mathcal{F}^{-1}\{q(\omega)\} &= q(t) = \frac{1}{2\pi} \int_{-\infty}^{\infty} q(\omega) \exp(i\omega t) d\omega, \end{aligned} \quad (14)$$

equation 12 becomes

$$\begin{aligned} &\left(\frac{\partial^2}{\partial y_i \partial y_i} + k^2 - 2iM_i k \frac{\partial}{\partial y_i} \right. \\ &- \left. M_i M_j \frac{\partial^2}{\partial y_i \partial y_j} \right) (H(f)c_o^2 \rho'(\mathbf{y}, \omega)) = \\ &\frac{\partial}{\partial y_i} (F_i(\mathbf{y}, \omega)\delta(f)) - i\omega Q_n(\mathbf{y}, \omega)\delta(f) \\ &- \frac{\partial^2}{\partial y_i \partial y_j} (T_{ij}(\mathbf{y}, \omega)H(f)). \end{aligned} \quad (15)$$

The wavenumber is defined by $k = \omega/c_o$, the Mach number $M = U/c_o$, and complex number $i = \sqrt{-1}$. Note that the transform has been applied to the groupings T_{ij} , F_i , and Q because the equation is linear in these terms. However, the desirable properties of the FW-H are maintained because all of the nonlinear products are included before the transformation is applied. In a numerical implementation, the products are formed first, and then a fast Fourier transform (FFT) is applied. As a caution, the FFT must use the sign convention of equations 14, or the derivation must be modified appropriately. The Green function for equation 15 when $M < 1$ can be obtained from a Prandtl-Glauert transformation. Denoting the three-dimensional source coordinates as (ξ, η, ζ) , and the observer position as (x, y, z) the Green function¹⁵ is

$$G(x, y, z; \xi, \eta, \zeta) = \frac{-1}{4\pi d} \exp(-ik(d - M\bar{x})/\beta^2)$$

where

$$\begin{aligned} \bar{x} &= (x - \xi) \cos \alpha \cos \phi + (y - \eta) \sin \alpha \\ &+ (z - \zeta) \cos \alpha \sin \phi, \\ \bar{y} &= -(x - \xi) \sin \alpha \cos \theta + (y - \eta) \cos \alpha \\ &+ (z - \zeta) \sin \alpha \sin \phi, \\ \bar{z} &= -(x - \xi) \sin \phi + (z - \zeta) \cos \phi, \end{aligned}$$

and

$$d = \sqrt{\bar{x}^2 + \beta^2(\bar{y}^2 + \bar{z}^2)} \quad (16)$$

The angles are defined such that $\tan \phi = W/U$, $\sin \alpha = V/M$, and $M = \sqrt{U^2 + V^2 + W^2}/c_o$. The Prandtl-Glauert factor is $\beta = \sqrt{1 - M^2}$. The solution to equation 15 for $M < 1$ can now be written as

$$\begin{aligned} H(f)c_o^2 \rho'(\mathbf{y}, \omega) &= - \int_{f=0}^{\infty} F_i(\boldsymbol{\xi}, \omega) \frac{\partial G(\mathbf{y}; \boldsymbol{\xi})}{\partial y_i} ds \\ &- \int_{f=0}^{\infty} i\omega Q_n(\boldsymbol{\xi}, \omega) G(\mathbf{y}; \boldsymbol{\xi}) ds \\ &- \int_{f>0}^{\infty} T_{ij}(\boldsymbol{\xi}, \omega) H(f) \frac{\partial^2 G(\mathbf{y}; \boldsymbol{\xi})}{\partial y_i \partial y_j} d\boldsymbol{\xi}. \end{aligned} \quad (17)$$

As has already been stated, the quadrupole contribution, represented by the last term in equation 17, is typically neglected because its influence is often small. Furthermore, the calculation is somewhat involved and expensive. Certain flows exist where the quadrupole cannot be ignored, such as those containing significant refraction of waves by shear layers and wakes. As long as the integration surface is placed outside of all regions where T_{ij} is large, the quadrupole contribution is substantially included by the surface sources even though the quadrupole integration is not performed. This is also true for the time-domain formulation.

The frequency-domain solution process involves calculating the surface normals and forming the products in F_i and Q for all time at each point on the surface just as in the time-domain version. However, the F_i and Q_n functions are Fourier transformed, and the surface integrations are performed for each frequency of interest instead of for each observer time. An inverse FFT can be used to recover the acoustic signal in the time domain. For truly periodic problems one merely uses a single period of the flow data as input to the FW-H code. However, for more complicated, aperiodic flows, windowing the data is required. The windowing should be applied to F_i and Q_n after their mean values are subtracted. The subtraction has no effect on the calculated noise because the derivatives of G all contain ω , and equation 17 shows that there is no contribution to the noise at $\omega = 0$ when the quadrupole term is neglected. The minimal amount of time data typically available from a computational aeroacoustics calculation may lead to some inaccuracies in the windowed FFT, but short time records are often just as much of an impediment for time-domain formulations because information about the frequency content is usually desired.

When the input to FW-H code is from a harmonic, linearized Euler solver, F_i and Q_n should also be linearized because the amplitudes from the linearized code may not be physical. If they are too large, the nonlinearities in the source terms can produce erroneous results. One must be careful when performing the linearization because the perturbation velocities u_i are not necessarily small. For instance, on a solid surface $u_i = -U_i$. Only a minor change in the code allows one to have a single code that is useful for input from linear and nonlinear flow solvers. The frequency domain approach is particularly efficient for harmonic data because only a single frequency needs to be calculated, and the FFT's do not need to be performed.

A disadvantage of this particular frequency-domain formulation is that the source and observer are always a fixed distance apart, and all Doppler effects are lost. In a time-domain calculation, the distance between the observer and the source can be changed for each time step to simulate a flyover condition. Most CFD computations and experiments are carried out in a laboratory frame with the ob-

server distances fixed, so this is not a major issue. However, comparisons with actual flight data should include the Doppler effects.

Impenetrable Surfaces

As was shown for the time-domain formulation, the frequency-domain version can also be significantly simplified when the input data is obtained on solid surfaces. For impenetrable surface data, $u_j = -U_j$ and equations 13 simplify to

$$Q = -\rho_o U_i \hat{n}_i \quad \text{and} \quad F_i = p \hat{n}_i. \quad (18)$$

Note that Q is steady in time and has no impact on the frequency domain solution. Hence, only the time history of the pressure is needed. One only needs to determine the Fourier transform of the pressure and scale that result by the appropriate normal to obtain the F_i terms. The savings in memory and computational requirements are so great that the solid surface formulation should be employed whenever possible. In the current implementation, different versions of two subroutines are called depending on the case being run. Although some additional coding is required, run times can be reduced by 60% and the memory load by over 70%.

Parallel Implementation

Although one normally thinks of acoustic analogy computations as being extremely efficient, calculations involving long time records and many observers can quickly become expensive. The cost of computing the time history at a single point using the FW-H may actually exceed that of a standard CFD method. However, the FW-H approach allows the observer location to be anywhere outside of the source region, whereas the CFD method must have grid points from the source to the observer. The cost involved with all those intermediate points and the errors incurred in the long range propagation make standard CFD an inappropriate choice for most far-field noise computations. Still, when mapping out the directivity in three-dimensions, hundreds of observer locations may be required. In the realistic problem of a landing gear given in the examples section, the FW-H computation of a single observer using the porous surface formulation requires seven minutes on an SGI 250MHz R10K processor. The input record contains 4096 time steps at 82,219 grid points, which consumes 1.4 GB of disk space. Mapping out a directivity is a time consuming process when performed serially. This motivated the modification of the code to use the Message Passing Interface (MPI) to perform parallel computations. Other researchers¹⁶ have used MPI in conjunction with acoustic analogy methods.

FW-H solvers are ideal candidates for parallelization because the calculation of the signal at each observer is independent, and the contributions from each portion of the

data surface combine linearly. Even the computations at each time step or frequency are independent. Hence, one has many choices of how to split the problem. Some initial testing was done with different processors dealing with different observers. However, this requires that each processor have access to the entire data record for all the surface patches. In the landing gear case, 181 patches comprise the total surface. Either all of the nodes have to read all the data, or one node must read it and broadcast it to all the others. The total record for the landing gear is expected to be over 10 GB on a medium mesh, and over 60 GB for a fine mesh. Either reading or passing that much data is not reasonable. This same problem occurs when different processors handle different frequencies or time steps. The other option is to divide the problem by surface patches, and sum all of the contributions at the end. Each processor only needs to read the data for the particular patches assigned to it. Hence, the data is only read once and only passed if the data is not directly accessible by all the nodes.

Two paradigms were used to investigate the parallel implementation. First, a standard load-balancing approach was used. The size of each of the patches was read, and the largest patch assigned to the processor with the least points until all the patches were assigned. This strategy is commonly employed in multiblock CFD codes. This approach worked well when all of the processors were identical and dedicated. However, because the code only passes a very minimal amount of data, it is typically run over a standard network on the second processor of SGI Octane workstations in the lab. These machines vary in speed, and sometimes both processors are in use when the job starts. Occasionally, one of the processors would take much longer than all of the others to complete. To circumvent this problem, the master-slave paradigm employed by Long and Brentner¹⁷ was used. Here, one node does no work other than to tell requesting nodes what patch they should process. Again, the largest patches are assigned first so that small patches are being used when the job nears completion and the variability in processor speed is important. This paradigm worked extremely well and has resulted in a nearly linear speed up on an SGI Origin. Although the master node does not do any useful work, it needs to respond quickly to the requests from worker nodes to keep them from becoming idle. The master's job can be assigned to a slow node or to a dual processor machine that also has a slave process.

In a heterogeneous environment where one is trying to use idle machines, the master-slave paradigm is preferred. Furthermore, the load-balanced approach and master-slave approach only affect a single subroutine in the code, so it is very easy to switch between the two depending on the local operating environment.

Test Examples

Monopole in Flow

As a first demonstration of the current implementations of the three-dimensional FW-H equation, the field from a monopole source is computed in the far field using the present technique. The source moves in the $-x$ direction at Mach 0.5. An equivalent flow involves a fixed source at the origin in a uniform flow in the $+x$ direction. The complex potential for the monopole is given by Dowling and Ffowcs Williams¹⁵ as

$$\phi(x, y, z, t) = A \frac{1}{4\pi d} \exp^{i(\omega t - k(d - Mx)/\beta^2)}. \quad (19)$$

The variables needed in the FW-H equation are obtained from the real parts of $p' = -\rho_o(\partial\phi/\partial t + U_o\partial\phi/\partial x)$, $u'_i = \partial\phi/\partial x_i$, and $\rho' = p'/c_o^2$. Equation 19 is written in a laboratory frame where the flow is moving over a stationary source. The source terms in the FW-H equation are calculated from the flow variables evaluated over two periods on the surface. For this case, $M = U_o/c_o = 0.5$, $\omega l/c_o = 4\pi/46$, $A/(lc_o) = 0.01$ and the integration surface is a cube that extends from $-5l$ to $5l$ in all three coordinate directions. The reference length is l . Fifty uniformly spaced points are used on each side of the box. Figure 1(a) compares the directivity from the calculations to the analytic solution in the $z = 0$ plane. Figure 1(b) makes a similar comparison for the time history at $(50l, 0, 0)$. The agreement is excellent, demonstrating that the formulations are valid for problems with a uniform mean flow. Similar agreement was found when each of the six sides of the cube comprising the data surface were deformed to look like a Gaussian bell provided enough points were provided to adequately resolve the variation. The calculations were performed in single precision, which appears sufficient as long as the acoustic signal on the surface is not less than five orders of magnitude smaller than the mean. A lack of smoothness in a time-domain formulation solution is an indication of a precision problem.

Landing Gear

This example involves the calculation of the noise generated by the unsteady flowfield surrounding a landing gear. An aerodynamic and acoustic analysis of a similar landing gear was performed by Souliez *et al.*¹⁸ The near field in this problem is highly nonlinear, and different parts shed vorticity at different frequencies. Figure 2(a) shows an instantaneous snapshot of the perturbation pressure on all of the solid surfaces. The freestream Mach number is 0.2, and the gear is mounted on a flat plate. The reference length is the diameter of the wheels which is 3.7 in (0.09398 m). The input data for the acoustic calculation is obtained from a three-dimensional, time-dependent

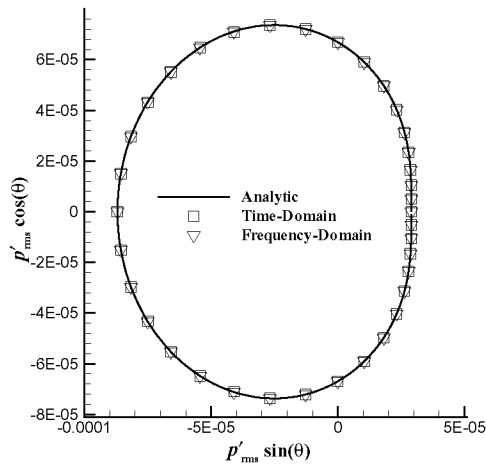
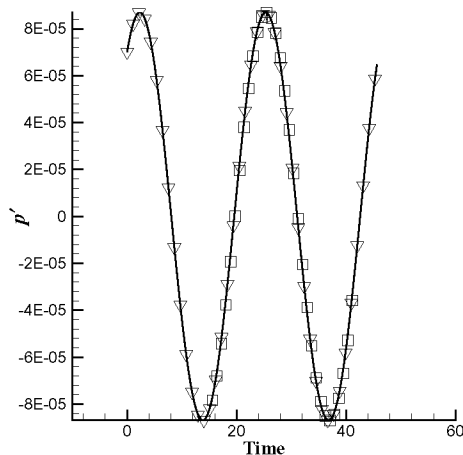
(a) Directivity at $r = 50l$ (b) Time history at $(50l, 0, 0)$

Fig. 1 Solution comparisons for a monopole in a $M = 0.5$ flow. The pressure is nondimensionalized by $\rho_0 c_0^2$

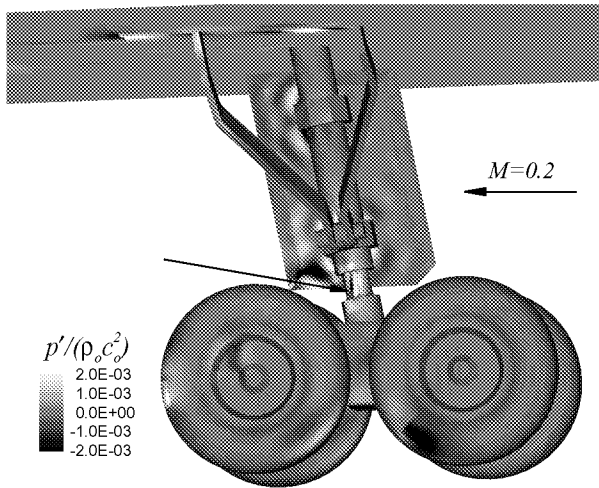
CFD solution using the code CFL3D.^{19,20} CFL3D was developed at NASA Langley Research Center to solve the three-dimensional, time-dependent, thin-layer Reynolds-averaged Navier-Stokes (RANS) equations using a finite-volume formulation. The CFD data used in this work is discussed in more detail in the paper by Li *et al.*²¹

The noise calculation involves 181 total patches comprising the data surface. All of the patches are on solid surfaces, so only the pressure histories are needed. 147 patches are on the gear itself and 31 are on the plate above the gear. So far, over 24,000 nondimensional time samples of $l/c_0 \Delta t = 0.02$ have been collected, but only half of the data is sufficiently free of transients to be useful for acoustic calculations. The transient problem is exacerbated by

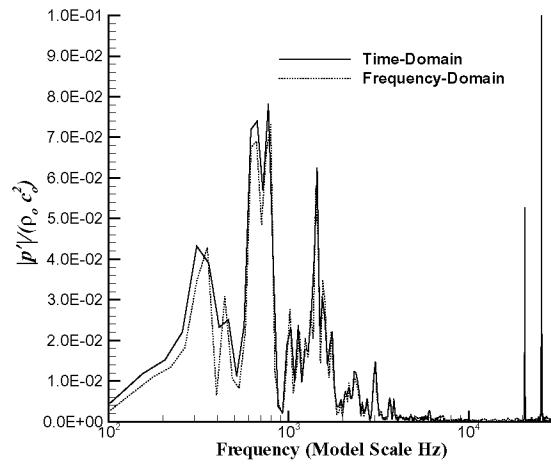
high-frequency sources that are growing through most of the time record. Some of the waves from these sources can be seen on the door in Figure 2(a). Figure 2(b) shows the time history of the pressure on the oleo in the contraction just below the door as indicated by the arrow in Figure 2(a). The time history shows the complex, intermittent character of the signal. The large amplitude oscillations occur around one kHz (model scale) at varying intervals and irregular durations. Riding on top of the signal are high frequency oscillations generated by resonances in small, triangular shaped spaces between the yokes and the door. These spaces are found on the upper and lower yokes in both the upstream and downstream junctures with the door. Unfortunately, the signals took a long time to saturate, so the calculation had to be run much longer than anticipated to eliminate the transients. The upstream and downstream cavities are slightly different in size, so the resonances occur at 20.5 kHz in the upstream cavity and at 25.4 kHz in the downstream one.

Beyond the intermittency in the signal, another complication for obtaining spectral information about the solution is the predominantly low frequency content of the gear. Very long sampling times are needed to resolve these frequencies. Although the time-domain code can exactly calculate the signal at the observer, the lack of long sampling times is a problem when the spectral content is needed. Nonetheless, the comparison of the spectra at an observer directly beneath the gear from the two FW-H codes is encouraging. The observer is $12l$ away from the gear. Figure 3(a) shows that the spectral content is nearly identical. In both cases, a hamming window was applied to minimize the effects of the aperiodic signal on the FFT's. The time histories in Figure 3(b) are also similar. The curves are offset because the frequency-domain calculation does not include the effect of the zero or steady mode. All of the primary features of the signal can be observed in both results. Some discrepancy should be expected because the effect of the window is already included in the frequency domain results because the window is applied to the input data. However, the window is applied to the time-domain results after the calculation, so its effect is not seen in Figure 3(b).

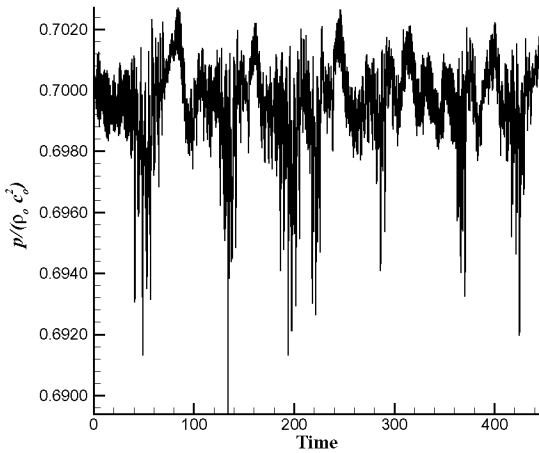
Three different data records were used to investigate the influence of the duration and the particular time interval used. Because of the complexity of the time histories on the gear, some variation should be expected, but drastic changes would indicate an improper sample length or that the flow has yet to eliminate transients. These sorts of variations were observed in many of the initial calculations. However, the comparison in Figure 4 shows only minor differences between the three calculations. A time sample of 8192 was used, which represents the time required for the flow to pass by a wheel 32 times. The full record was used, then it was subdivided into two records of 4096 samples.



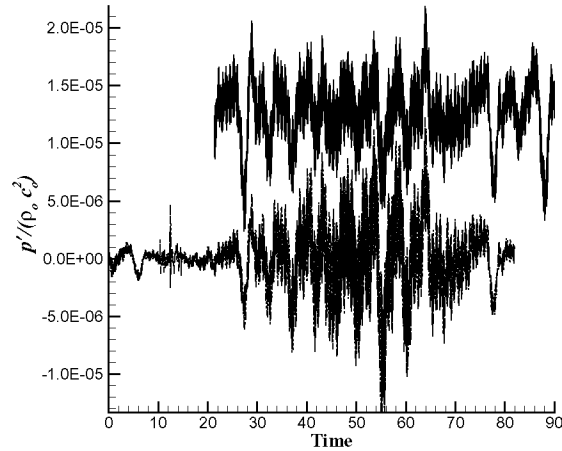
(a) Perturbation pressure on solid surfaces



(a) Spectra



(b) Time history on the oleo



(b) Time history

Fig. 2 CFD results for a landing gear in a $M = 0.2$ flow.

Fig. 3 FW-H results for an observer directly below a landing gear in a $M = 0.2$ flow.

The comparison between the results for the full record and the latter record is very good. Somewhat more discrepancy is observed with the results for the first 4096 samples, but it is still within the variation that should be expected for such a complex flow. Even though there are not as many samples available from the computation as one can obtain from an experiment, the power spectral density should be calculated by averaging over the different samples to obtain a single answer, which should be stationary.

One of the concerns with the CFD calculation was the accuracy of the solution on the wall above the landing gear. Although the plate doesn't produce any significant fluid mechanic fluctuations that would act as sound sources, it does reflect acoustic signals, and some of the vorticity shed by the side bars interacts with the wall. The grid on the

plate in the CFD calculation coarsens very quickly away from the gear, so the accuracy of high frequency signals is likely to be very poor over much of the plate. To investigate the impact of the accuracy on the plate, the FW-H solvers were run with the wall ignored and the gear surfaces mirrored about the plate. Figure 5 shows the comparison with results obtained by including and excluding the wall. At lower frequencies, the case including the wall has much higher levels than either the no wall or mirrored cases indicating that the signal on the wall is an important source of noise. The results in the figure are from the frequency-domain code, but very similar results were obtained from the time-domain code. Figure 5(b) zooms in on the high frequency tones. For the tones, the wall and no wall re-

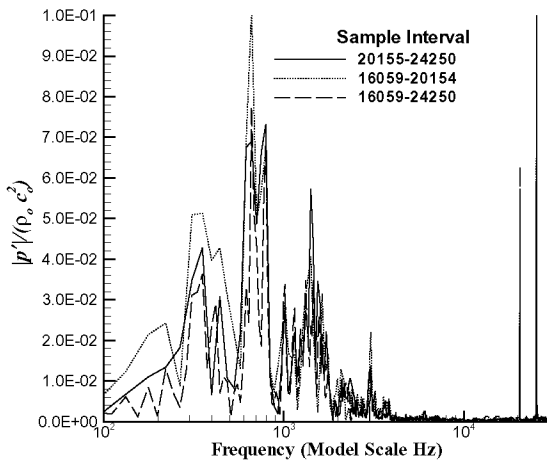
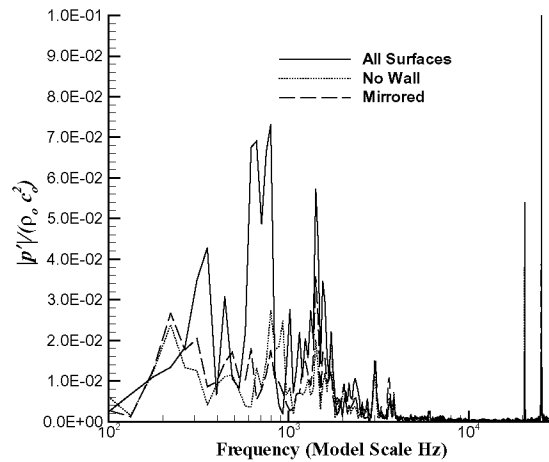


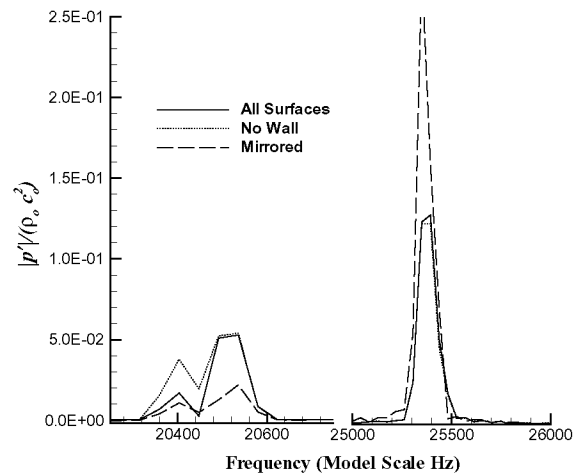
Fig. 4 FW-H results for an observer directly below a landing gear in a $M = 0.2$ flow. Calculations from frequency-domain code comparing effect of sample length.

sults are nearly identical which supports the idea that the high-frequency signals on the wall are artificially dampened rapidly so that they have little impact on the acoustic calculation. The mirrored result is lower at 20.5 kHz and significantly higher at 25.4 kHz. The variability in the effect of mirroring with frequency is likely caused by interference effects which would be minimized for observers farther from the gear.

Because of the complexity of the landing-gear geometry and the various locations of the sources, one would expect the observer location to be important. Figure 6 compares the spectra for observers at three locations. All of the observers are 12l from the gear. The first location is directly beneath the gear. The other two observers are at the same vertical and streamwise locations as the wheels, but on opposite sides. The observer on the oleo side doesn't have the door in the way to obscure some of the sources on the oleo and yokes. This is most evident for the 25.4 kHz tone in Figure 6(b). Both side observers see much stronger tone signals indicating that the yoke resonances primarily radiate horizontally. Part of the reason that the strength of the tones observed underneath the gear is much less may be because of blockage by the truck and wheels. The 20.5 kHz tone has the same amplitude for both side observers. The reason for the lack of influence of the door on this tone has not been investigated. At lower frequencies, the signal beneath the gear has a larger amplitude indicating that the wheels and truck are best observed from below. The portion of the signal around 1.4 kHz is completely absent for the side observers. As expected, there is a significant directivity associated with the gear, but the complex interplay of source location, geometry, and observer position needs further investigation.



(a)

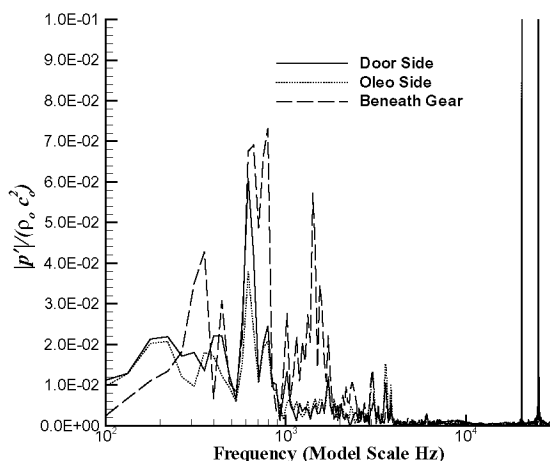


(b)

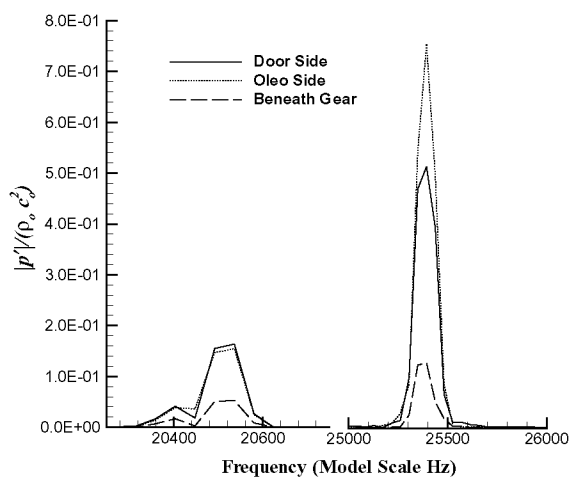
Fig. 5 FW-H results for an observer directly below a landing gear in a $M = 0.2$ flow. Results from frequency-domain code comparing the effect of including the wall and mirroring the data.

Performance

In the landing gear calculations, all of the frequencies were calculated in the frequency domain code, and an equivalent number of time steps in the time domain code. Table 1 shows timing results for the serial runs with 4096 samples and all 181 surfaces. These calculations involved solid surface data, so the impenetrable surface simplifications were employed. Run times are more than doubled if the surface is assumed to be penetrable. All of the frequencies were calculated by the frequency-domain code, and an equivalent number of observer times in the time-domain code. When all of the data is computed, the frequency-



(a)



(b)

Fig. 6 FW-H results for an observer directly below a landing gear in a $M = 0.2$ flow. Results from frequency-domain code comparing the effect of observer location. All observers are $12l$ from the gear. The side observers have the same vertical location as the wheels.

domain code is considerably faster. However, the ordering of the input data was kept the same for both codes so they could share input files. The ordering used is more natural for the frequency-domain code which must perform FFT's on the time records. The time-domain code must interpolate the source terms to the retarded time, and this is done much more efficiently when the data is ordered such that the variable index varies fastest. The current code rearranges the data internally to obtain the preferred ordering. Even accounting for this extra work, the frequency-domain code would still be more efficient. Furthermore, the gear

spectra is primarily concentrated at low frequency and at a few select tones. The number of frequencies computed could be significantly reduced in the frequency domain code. However, fewer temporal samples could be calculated in the time-domain code as long as the tones could be neglected. The time-domain code also has the advantage that one only needs to calculate the new portions of the observer signal as new input data is made available. Because the FFT's are performed on the input for the frequency-domain code, there is a minimum sample length necessary to produce reasonable results.

Code	CPU Time (s)
Time Domain	1089
Frequency Domain	425

Table 1 CPU time comparison of serial computations of a landing gear signal for one observer from 4096 time samples on 181 patches with 82,219 grid points. Calculations performed on a 250 MHz, R10k SGI Octane.

Code	Observers	CPU Time (s)
Time Domain	1	88.0
	3	128.1
Frequency Domain	1	56.5
	3	85.0

Table 2 CPU time comparison of parallel computations of a landing gear signal from 4096 time samples on 181 patches with 82,219 grid points. Sixteen SGI Octane worker nodes of nonuniform speed were used in the master-slave calculations.

For problems the size of the landing-gear calculation, the computations are normally performed in parallel using MPI. Because of the high utilization of machines dedicated for parallel calculations, the master-slave paradigm was used to take advantage of the second processor on sixteen SGI Octanes in the lab. The processor speeds varied from 195 to 250 MHz. The master node was attached to a RAID system that stored the input data. Table 2 shows the timing results for calculations involving one and three observers. The speedup from the serial case is clearly not linear, but the run times have been significantly reduced. Furthermore, much of the time is spent doing file input and output. The master node is not capable of reading the data fast enough to satisfy all of the worker nodes. In this problem, a total of 1.4 GB of data must be read and transferred across the network. When the code first starts, all of the worker nodes simultaneously try to access their data from the master. Distributing the data before the calculation would be more efficient, but having the data in one place is much more convenient. Furthermore, as the number of observers increases, the work to disk access ratio improves resulting in better efficiency as can be seen from the three observer cases in table 2. The point of this example is not to show that perfect efficiency has been obtained,

but rather to demonstrate that the MPI implementation has enabled directivity mappings of thousands of observer locations to be performed relatively quickly on machines that are typically idle.

Conclusions

Two different formulations of the three-dimensional Ffowcs Williams and Hawkings equation for sources in uniform, subsonic, rectilinear motion have been presented. They are efficient enough to be used to perform far-field predictions from large data sets provided by either computation or experiment. Comparisons of the solutions for two example problems showed excellent agreement between the frequency- and time-domain formulations. Although the frequency-domain version of the code is somewhat faster, both algorithms are efficient enough to be used for computations involving large data sets when MPI is used to distribute the problem to many computers. Each formulation has different advantages that make it more attractive for certain classes of problems, but our tests have shown that they produce basically equivalent results for the problems investigated.

References

- ¹Ffowcs Williams, J. E. and Hawkings, D. L., "Sound generation by turbulence and surfaces in arbitrary motion," *Philosophical Transactions of the Royal Society of London A*, Vol. 342, 1969, pp. 264–321.
- ²Singer, B. A., Lockard, D. P., Brentner, K. S., and Lilley, G. M., "Simulation of Acoustic Scattering from a Trailing Edge," *Journal of Sound and Vibration*, Vol. 230, No. 3, 2000, pp. 541–560.
- ³Brentner, K. S. and Farassat, F., "An Analytical Comparison of the Acoustic Analogy and Kirchhoff Formulation for Moving Surfaces," *AIAA Journal*, Vol. 36, No. 8, 1998, pp. 1379–1386.
- ⁴Lyrantzis, A. S., "The Use of Kirchhoff's Method in Computational Aeroacoustics," *ASME Journal of Fluids Engineering*, Vol. 116, 1994, pp. 665–675.
- ⁵Baeder, J. D., Gallman, J. M., and Yu, Y. H., "A Computational Study of the Aeroacoustics of Rotors in Hover," *Journal of the American Helicopter Society*, Vol. 42, No. 1, 1997, pp. 39–53.
- ⁶Di Francescantonio, P., "A New Boundary Integral Formulation for the Prediction of Sound Radiation," *Journal of Sound and Vibration*, Vol. 202, No. 4, 1997, pp. 491–509.
- ⁷Strawn, R. C. and Biswas, R., "Computation of Helicopter Rotor Noise in Forward Flight," *Journal of the American Helicopter Society*, Vol. 40, No. 3, 1995, pp. 66–72.
- ⁸Farassat, F., "Linear Acoustic Formulas for Calculation of Rotating Blade Noise," *AIAA Journal*, Vol. 19, No. 9, 1981, pp. 1122–1120.
- ⁹Lockard, D. P., "An Efficient, Two-Dimensional Implementation of the Ffowcs Williams and Hawkings Equation," *Journal of Sound and Vibration*, Vol. 229, No. 4, 2000, pp. 897–911.
- ¹⁰Crighton, D. G., Dowling, A. P., Ffowcs Williams, J. E., Heckl, M., and Leppington, F. G., *Modern Methods in Analytical Acoustics*, chap. 11, Springer-Verlag, London, 1992.
- ¹¹Farassat, F. and Succi, G. P., "The Prediction of Helicopter Discrete Frequency Noise," *Vertica*, Vol. 7, No. 4, 1983, pp. 309–320.
- ¹²Garrick, I. E. and Watkins, E. W., "A Theoretical Study of the Effect of Forward Speed on the Free Space Sound Pressure Field Around Helicopters," TR 1198, NACA, 1954.
- ¹³Cook, R., Malkus, D., and Plesha, M., *Concepts and Applications of Finite Element Analysis*, chap. 6, John Wiley & Sons, Inc., 1989, pp. 176–180.
- ¹⁴Guo, Y., "Application of the Ffowcs Williams/Hawkings Equation to Two-Dimensional Problems," *Journal of Fluid Mechanics*, Vol. 403, January 2000, pp. 201–221.
- ¹⁵Dowling, A. P. and Ffowcs Williams, J. E., *Sound and Sources of Sound*, chap. 9, Horwood Publishing, Westergate, 1983, pp. 207–208.
- ¹⁶Ozyoruk, Y. and Long, L. N., "A New Efficient Algorithm for Computational Aeroacoustics on Parallel Computers," *Journal of Computational Physics*, Vol. 125, 1996, pp. 135–149.
- ¹⁷Long, L. N. and Brentner, K. S., "Self-Scheduling Parallel Methods for Multiple Serial Codes with Application to Wopwop," AIAA-2000-0346, 1996, Presented at the 38th AIAA Aerospace Sciences Meeting, Reno, NV, Jan 10-13.
- ¹⁸Souliez, F. J., Long, L. N., Morris, P. J., and Sharma, A., "Landing Gear Aerodynamic Noise Prediction Using Unstructured Grids," AIAA Paper 2002-0799, Presented at the 40th AIAA Aerospace Sciences Meeting, Reno, NV, Jan 14-17, 2002.
- ¹⁹Rumsey, C., Biedron, R., and Thomas, J., "CFL3D: Its History and Some Recent Applications," TM 112861, NASA, May 1997, presented at the Godonov's Method for Gas Dynamics Symposium, Ann Arbor, MI.
- ²⁰Krist, S. L., Biedron, R. T., and Rumsey, C., "NASA Langley Research Center: Aerodynamic and Acoustic Methods Branch," *CFL3D User's Manual (Version 5)*, 1997.
- ²¹Li, F., Khorrami, M. R., and Malik, M. R., "Unsteady Simulations of a Landing-Gear Flow Field," AIAA Paper 2002-2411, Eighth AIAA/CEAS Aeroacoustics Conference, Breckenridge, CO, June 17–19, 2002.